White-light driven resonant emission from a monolayer semiconductor

Shang, Jingzhi; Wu, Lishu; Feng, Shun; Chen, Yu; Zhang, Hongbo; Cong, Chunxiao; Huang, Wei; Yu, Ting

2022

Title: White-Light Driven Resonant Emission from a Monolayer Semiconductor

Jingzhi Shang, Lishu Wu, Shun Feng, Yu Chen, Hongbo Zhang, Chunxiao Cong, Wei Huang*, and Ting Yu**

Prof. J. Shang. Prof. W. Huang

Shaanxi Institute of Flexible Electronics (SIFE), Northwestern Polytechnical University (NPU), Xi'an 710129, China

E-mail: iamwhuang@nwpu.edu.cn

L. Wu, Dr. S. Feng, Dr. Y. Chen, H. Zhang, Prof. T. Yu

Division of Physics and Applied Physics, School of Physical and Mathematical Sciences, Nanyang Technological University, Singapore 637371

E-mail: yuting@ntu.edu.sg

Prof. C. Cong

State Key Laboratory of ASIC and System, School of Information Science and Technology, Fudan University, Shanghai 200433, China

E-mail: cxcong@fudan.edu.cn

Prof. W. Huang

Key Laboratory of Flexible Electronics and Institute of Advanced Materials, National Jiangsu Synergetic Innovation Centre for Advanced Materials, Nanjing Tech University, Nanjing 211816, China

Prof. T. Yu

School of Physics and Technology, Wuhan University, Wuhan 430072, China

Abstract: Resonant emission in photonic structures is very useful to construct all-photonic circuits for optical interconnects and quantum computing. Optical generation of most resonant emitting modes in photonic structures has been obtained by coherent pumping rather than incoherent illumination. Particularly, the development of white-light or even solar-powered on-chip light sources remains challenging but is very attractive in view of the much facile availability of these incoherent excitation sources. Here the net resonant emission from monolayer semiconductor has been demonstrated under the simulated solar illumination by a white light-emitting diode. The device is formed by embedding a two-dimensional gain medium into a planar microcavity on a silicon wafer, which is compatible with the prevailing on-chip photonic technology. Coherent and white-light excitation sources are respectively selected for optical pumping, where the output light in two cases exhibits the well-consistent resonant wavelength, linewidth, polarization, location, and Gaussian-beam profile. The fundamental TEM_{00} mode behaves a doublet emission, resulting from anisotropy-induced nondegenerate states with orthogonal polarizations. The extraordinary spectral flipping is attributed to the competitive interplay of resonant absorption and emission. This work paves a way towards white-light or solar-powered state-of-the-art photonic applications at the chip scale.

Introduction

Two-dimensional (2D) semiconductors with direct bandgaps have attracted much attention due to their robust optical properties,[1] which open many opportunities to develop the next generation of on-chip photonic applications such as optical interconnects and quantum information. In particular, on-chip light sources are one of the most important building blocks for the promising integrated all-photonic circuits. Nowadays, optically driven light sources based on 2D semiconductors have been developed such as small lasers,[2, 3] single-photon emitters[4], resonant photon emitters,[5-8], optical parametric amplifiers[9], and other emitters[10] based on second-harmonic generation processes, in which all these emitters require coherent optical pumping by additional laser sources. Employing these laser excitation sources complicates practical integration and miniaturization of all-photonic circuits. Alternatively, incoherent solar irradiation is one of the most promising energy sources in view of environment-friendly nature and facile availability, which has been utilized to optically driven optoelectronic and photonic devices, such as solar cells[11] and macroscale solar-pumped light sources.[12-15] Hence, building microscale solar-driven light sources based on the new generation of 2D semiconductors will be appealing for on-chip all-photonic applications. Nevertheless, such photonic

device architectures have not caused enough attention and spectroscopic features of light emission from 2D semiconductors under solar or white-light illumination remain unclear.

Previously, the majority of solar-powered light sources have been developed by using large device architectures,[13-17] such as centimeter long Nd:YAG crystals,[16] tens of meter long doped fibers,[18] spacious lens[14], and mirrors,[15] which significantly limit microscale applications of these solar-powered light sources. Moreover, the fabrication processes of traditional solar-powered light sources mismatch with the silicon planar technology and greatly hinder their miniaturization and integration for on-chip applications. Nowadays, direct bandgap 2D semiconductors together with ultrathin planar microcavities provide new opportunities to overcome the development issues of miniaturized solar pumped light emitters. Here, with the help of an ultrathin planar microcavity grown on a SiO_2/Si substrate, we have demonstrated monolayer semiconductor resonant emission under the simulated solar illumination. Two excitation sources of a laser and a white light-emitting diode (LED) have been respectively used for optical pumping to address the resonant emission nature. Furthermore, unconventional spectroscopic characteristics of light emission from 2D semiconductors have been revealed under incoherent optical pumping.

Results

Figure 1a presents the schematic of a miniaturized solar-pumped resonant-emitting device employing a 2D semiconductor microcavity, which consists of the emitting layer, dielectric spacers, and distributed Bragg reflectors (DBRs). The direct bandgap semiconductor of monolayer WS_2 (1L-WS_2) was embedded at the center of a planar half-wavelength SiO_2 cavity sandwiched by the top and bottom SiO_2/TiO_2 DBRs, and the whole microcavity structure was deposited on a 300 nm-SiO_2/Si wafer. Figure 1b shows optical images of atomically thin WS_2 flakes on the half resonant cavity (left panel) and embedded in the full cavity (right panel), respectively, where the monolayer region is indicated by the white dashed frame. The solar light was simulated by a white LED whose illumination profile (Fig. 1c) was obtained by monitoring its reflected signals from an Ag-coated mirror. The photoluminescence (PL) spectrum of 1L-WS_2 and the normal reflection spectrum of the

blank microcavity are shown in Fig. 1d together, where a single reflection dip appears around the center and the PL peak is fully within the stopband. In other words, such design can confine nearly all emission from 1L-WS$_2$ except the designed cavity mode, which is beneficial to reduce the leaked spontaneous emission (LSE) and thus minimizes the optical loss. The zoom-in reflection spectrum (Fig. 1e) around the dip indicates a single cavity mode of C$_0$ at 654 nm (corresponding to 1.896 eV) with a narrow width of 0.32 nm, and thus a quality (Q) factor of $\lambda/\Delta\lambda \approx 2040$ is estimated for the blank microcavity. Consequently, the resonant emission is anticipated to take place under conventionally optical pumping by a laser source. Note that, here the cavity mode is intentionally designed to be located at the low energy tail of the excitonic emission of 1L-WS$_2$, which not only aims to reduce the absorption loss in the microcavity but also to drive the light-matter coupling in the weak coupling regime to obtain the resonant emission enabled by Purcell effect[19] rather than the cases[20] in the strong coupling regime.

Indeed, here we not only determined resonant emission features of 1L-WS$_2$ embedded microcavity under laser excitation but also further explored fine optical response in the spectral region of cavity resonance under white-light illumination. Figure 2a presents the unpolarized PL spectrum from 1L-WS$_2$ embedded microcavity, where a sharp doublet emission sits on the broad LSE profile. By fitting with the double Lorentzian function, two emission components are extracted at 659.0 and 659.5 nm with the narrow linewidths of 0.25 and 0.23 nm, respectively. Note that, with an isotropic active medium, the fundamental transverse electromagnetic mode (TEM$_{00}$) of a vertical microcavity shall contain two linear and orthogonal polarization states.[21] Therefore, the observed doublet peak is attributed to the fundamental mode of TEM$_{00}$ with two polarization states, where the nondegenerate emission energies are due to the presence of transverse anisotropies originating from the device materials or structures. Previously, similar anisotropy-induced splits of emission energies were also observed in AlGaAs quantum-well microcavity devices.[22] In our case, the emission-wavelength variations of the TEM$_{00}$ mode are less than 0.2 nm, which are mainly limited by the spectral resolution, the fit error, and the unintentional fluctuation of cavity thickness. Moreover, with the help

of a linear polarizer, the PL polarization has been clarified by monitoring the emission along x (0°) and y (90°) directions as indicated in the inset of Fig. 1b. The sharp components at 659.5 and 659.0 nm show the well-recognized horizontal and perpendicular polarizations, respectively, while the LSE band remains the same profile under two detection configurations (Fig. 2b). Although rotating the sample by a relative angle of about 20° to the incidence laser polarization, the linear polarizations of L_1 and L_2 stay respectively along x and y directions (Supplementary Fig. S1), which support the lifting degeneracy of polarization resulting from the device itself rather than the excitation polarization. Specifically, we consider three possible anisotropic origins of the doublet emission: the cavity-structure segment without the gain medium, the laser excitation polarization, and the structure of $1L$-WS_2. Firstly, the blank microcavity shows a single reflection dip (Figure 1e), indicating that the blank microcavity itself is isotropic in the surface plane and cannot account for the presence of anisotropy. Secondly, if the anisotropy is only induced by the laser excitation polarization, the expected polarization behavior should be unchanged after rotating our microcavity device. Nevertheless, the emission polarization behavior changes after the device rotation as shown in Figure S1, and thus the observed anisotropy is not caused by the laser excitation polarization. Thirdly, previous studies[22-24] on III-V semiconductor microcavities have suggested that the polarized emission features correlate with the structure of the gain medium, such as material birefringence or anisotropy,[22] anisotropic transverse geometry,[23] and certain crystal orientations of the gain media.[24] Therefore, the structure of $1L$-WS_2 may cause the observed polarization behavior. Here, we attribute the polarized doublet emission to the presence of anisotropy induced by the insertion of the gain medium, which is possibly related to the structure of $1L$-WS_2. Furthermore, we extend linearly polarized PL measurements covering -90 to 90°. Figure 2c presents the 2D plot of PL intensity *versus* wavelength and polarization angle, which verifies the doublet emission only containing two orthogonal components and also differs from the polarization-independent LSE (Supplementary Fig. S2). As a result, the observed narrow linewidth and the linear polarization are two resonant emission characteristics.

Figure 2d shows the unpolarized reflection signals under white-light illumination from the 1L-WS_2 embedded microcavity and the protected Ag mirror, respectively, where the dominant reflection backgrounds are equivalent in two cases and suggest the near-unity reflection of the microcavity in the most spectral regions. In the follow-up, the normalized reflection signals have been collected from blank and 1L-WS_2 embedded microcavities under two detection polarizations. In the spectral data collected at 0 or 90º, a dip appears and results from the cavity-mode (C_0) of the blank microcavity (Fig. 2e) while the flipping signal presents for 1L-WS_2 embedded microcavity, attributing to the spectral overlapping of the cavity-mode induced absorption of 1L-WS_2 embedded region and the sharp emission caused by the white-light illumination (Fig. 2f). In contrast to the C_0 position of the blank microcavity, the redshift of the cavity-mode induced dip (C_1 or C_2) in 1L-WS_2 embedded microcavity is due to the increase in the cavity length caused by the insertion of 1L-WS_2.[3] After removal of the background signal, the zoom-in flipping signal under the unpolarized configuration consists of two emission peaks of P_1 and P_2 and the nearby dips of C_1 and C_2 (Fig. 2g). The emission signal of P_1 or P_2 correspondingly pops up with the C_1 or C_2 dip at the collection polarization of 0 or 90º, respectively (Fig. 2h). As shown in the polarized spectral map (Fig. 2i), P_1 and P_2 together with the correlated C_1 and C_2 present linearly polarized behaviors, which are in accordance with the cases for L_1 and L_2, respectively (Fig. 2c).

Here we are interested in the origin of the flipping signal (P_1-C_1) consisting of P_1 and C_1 collected at 0º. Note that, the emission wavelength, the polarization, and the width (illustrated later in Fig. 3h) of P_1 observed under white-light illumination agree well with the ones of L_1 under laser excitation, which are pointed to the same resonant emission nature. Subsequently, the intensity decay processes of LSE and L_1 have been examined by performing confocal PL along the out-of-plane (Z) direction. With the detection plane away from the device surface (Z=0 μm), both LSE and L_1 remain at the same emission wavelengths. The intensity of LSE rapidly decreases (Fig. 3a) while the case of L_1 shows the longer propagation along the designed emitting direction (Fig. 3b). More clearly, the integrated intensities of LSE and L_1 along the Z-direction have been extracted and normalized as

shown in Fig. 3c. By fitting with the single exponential decay function, the estimated decay constants of L_1 and LSE are 4.1 and 2.1μm, respectively. Here the observed longer propagation of L_1 indicates the presence of more stable and less diffused output light along the Z direction, which is as expected for a vertical emitting resonant mode rather than the cases of LSE and spontaneous emission. In addition, the emission profiles of L_1 and L_2 along the Z-direction are analogous when detected in the unpolarized confocal PL configuration (Supplementary Fig. S3). In other words, these slow PL damping features along the Z-direction stand for the nature of the doublet resonant emission.

Meanwhile, the confocal optical response of the flipping signal was also examined under white-light illumination (Fig. 3d). The P_1 band shows a longer decay than that of LSE observed under laser excitation (Fig. 3a) and the C_1 dip displays the exotic evolution with the Z-position. The relevant spectra at various Z-positions are illustrated in Supplementary Fig. S4, which can be well reproduced by a combinational function taking a Lorentzian peak and a Breit-Wigner-Fano profile into account and the detailed fit results of spectra are shown in Supplementary Fig. S5. By use of such fit procedures, the 2D plot of simulated confocal signals is built (Fig. 3e), which finely duplicates the experimental observations (Fig. 3d). For comparison, the confocal reflection response of C_0 has also been measured and fitted as seen in Supplementary Fig. S6, in which the negative dip feature remains the same position from the surface up to 12 μm, as supposed for the cavity-induced absorption in the blank microcavity. Furthermore, integrated intensities, wavelengths, and widths of P_1 and C_1 as functions of Z-position are illustrated in Fig. 3f-h, respectively. The representative signals at 0.5 and 3.5 μm show the clear superpositions of P_1 and C_1 components while the one at 7.5 μm is dominated by a single dip of C_1 (see Supplementary Fig. S5). Both absolute integrated intensities of P_1 and C_1 components decrease from the surface position (*i.e.* 0 μm) to 5 μm. After that, the P_1 nearly disappears and the C_1 signal lasts till more than 10 μm (Fig. 3f). Both spectral positions are relatively stable below 5 μm while the one of C_1 obviously blueshifts after 5 μm (Fig. 3g) and approaches the ones of P_1, indicating the same cavity-resonant origin. In Fig. 3h, the width of C_1 gets narrow after P_1 evanesces and the linewidth of P_1 is slightly smaller than the one of C_1 at the same confocal plane

below 5 μm. As illustrated above, under confocal white-light illumination, the cavity mode of C_1 dominates at the Z-position away from the surface (>5 μm) while the narrower P_1 appears together with C_1 at the positions closer to the device surface.

Lastly, we examined the directionality and spatial coherence of the narrow spectral features *via* angle- and spatial-resolved reflection and PL measurements. Figure 4a presents angle-resolved reflection signals of C_0 from the blank microcavity measured at collection angles from -15 and 15°, in which the photon energy exhibits a parabolic dispersion in the in-plane momentum space, as predicted for the cavity photon.[25, 26] The corresponding angle-resolved reflection spectra are presented in Supplementary Fig. S7a. Note that, both bands of C_0 and LSE around k=0 obey the similar dispersion relationships in the weakly coupled regions with the negative detuning (*i.e.,* E_{ex}-E_{cav} <0).[26] Distinct from the dispersive traits of C_0, the angle-resolved PL map of L_1 presents a stable photon energy centered at 0° in a smaller momentum range (Fig. 4b), which is also seen in the related PL spectra (Supplementary Fig. S7b). More quantitively, the integrated intensities of L_1 between -10° and 10° are normalized and illustrated in Fig. S8, in which the angle-dependent distribution follows a Gaussian distribution with a divergence angle of ~10.4^o and indicates the formation of directional emission. The similar directional radiation with a reduced divergence has also been observed in perovskite-nanocrystals embedded microcavities and GaAs-based microcavities, supporting the evolution from uncoupled spontaneous emission, cavity-coupled spontaneous emission to even lasing.[27] Thus, our angle-resolved spectral data support the presence of the emission directionality (*i.e.,* vertical-emitting), which is a fingerprinting feature of resonant emission. Moreover, linearly polarized PL mappings of L_1 (Fig. 4c) and L_2 (Supplementary Fig. S9) from 1L-WS$_2$ embedded microcavity have been respectively collected under the excitation power density of 10.5 W/cm^2, in which both emission bands of L_1 and L_2 exhibit the spatially steady profiles and overlap at the same location. To further address the spatial character of the emission intensity, the line scanning of PL has been performed across the TEM$_{00}$ center at an elevated power density of 31.5 W/cm^2 (Supplementary Fig. S10). Previous studies have linked the Gaussian-distributed profiles of the fundamental transverse modes in

8

planar microcavities[21, 28] and the cavity modes in microdisks with the presence of Resonant emission beam.[8] Indeed, the intensity distributions of L_1 (Fig. 4d) and L_2 (Supplementary Fig. S10c) mostly follow the Gaussian functions as expected for the fundamental TEM_{00} mode, which is also evidence for the buildup of the spatially coherent beam. [8, 21, 28] The single-Gaussian fitting of the normalized intensity profile of L_1 gives a beam radius ω_0 of 1.1 ± 0.1 μm. A Gaussian-beam divergence can be estimated by $2\lambda/\pi\omega_0$ according to a previous definition[29], where λ is the emission wavelength (*i.e.* ~659.5 nm for L_1). As a result, the calculated beam divergence of L_1 is $11\pm1°$, which is well in line with the beam divergence (Fig. S8) measured by angle-resolved PL above. Figure 4e,f present the integrated intensity profiles of C_1 and P_1 from the 1L-WS$_2$ embedded microcavity under the while light illumination, which have been collected from the same area as the case (Fig. 4c) under laser excitation. The intensity profiles across the centers of C_1 and P_1 can be reproduced by use of a Gaussian function as shown in Supplementary Fig. 4g and 4h, respectively. Hence, both intensities of C_1 and P_1 present the similar Gaussian distributions with the one of L_1 at the identical position, indicating the consistent spatial coherence and location under both laser and white-light excitation conditions. In short, here both directional radiation and Gaussian-beam formation support the presence of spatial coherence[30] in our microcavities.

Discussion

White-light driven resonant emission

Under optical pumping by a laser, the resonant emission of L_1 from 1L-WS$_2$ embedded microcavity with a high Q factor is verified by narrow linewidth, linear polarization, less divergence supported by slow emission decay, angle-independent emission energy, vertical directionality, and spatial coherence verified by the formation of the Gaussian beam. Here, we focus on understanding the nature of P_1 under white-light illumination. Firstly, the emission wavelength, the linewidth, and the linear polarization of P_1 agree well with the ones of L_1. These features point to the same emission nature of P_1 and L_1. Secondly, the flipping P_1-C_1 signal can be interpreted referring to previous studies

on emission processes[31] and absorption transitions involving Fano-like interference[32]. As illustrated in Fig. 4i, a scheme consisting of three energy states is proposed, where S_1, S_2, and S_3 represent a low-lying state, a discrete excited state, and a continuum state, respectively. The flipping signal results from the interplay of two overlapping processes: a downward emissive transition from S_2 to S_1 and a combinational absorption component due to the Fano-like interference between two upward absorptive transitions of S_1 to S_2 and S_1 to S_3. Both S_2 and S_3 locate at the similar energy levels and the Fano-like interference causes the shift of absorption dip. At the middle crossing wavelength (*i.e.* indicated by the red circle in Fig. 4i) of such a flipping signal, this device is totally reflective since the cavity-mode induced absorption is canceled by the downward emission. At the spectral ranges above or below the crossing wavelength, the downward emission process of S_2 to S_1 or the combinational absorption process becomes prevailing, respectively. The transitions between S_1 and S_2 originate from the narrow resonant mode while the transition from S_1 to S_3 is associated with the weak excitonic absorption of $1L-WS_2$ at the low-energy tail[33]. Thirdly, the intensity distributions of L_1 and P_1 follow the Gaussian profiles and spatially coincide with each other. Such Gaussian-like shapes across the transverse cross-section, *i.e.,* parallel to the device surface, indicate the formation of a beam through the spatial coherence of monochromatic light output.[21] All these observations support the identical emission nature of P_1 and L_1. In a word, the narrow band of P_1 is attributed to the resonant emission enabled by white-light illumination.

Previously, by using 2D[34, 35] and 1D[7] photonic crystal nanocavities with varied 2D semiconductors, cavity-coupled exciton[34] or interlayer exciton[35] emission have been observed due to Purcell enhancement. In 2014, 2D-semiconductor incorporated vertical Fabry-Perot cavities with planar and concave mirrors have been employed to achieve tunable resonant emission at 4.2K.[36] With microdisk[5, 6, 8, 37] and microsphere[38] resonant cavities, whispering-gallery-mode emissions from 2D semiconductors have been obtained in the visible and infrared spectral regions. By comparison, the resonant emission features of 2D semiconductors have been further addressed as follows. First of all, distinct from the resonant emission[5-8, 34, 35-38] excited by coherent lasers

mentioned above, we have demonstrated resonant emission under incoherent optical pumping by a white LED. Moreover, being analogous to the cases in previous resonant emitters,[6-8] the measured Q factor of our microcavity device is high enough and the resultant linewidth of P_1 is smaller or comparable with the resonant emission bands of 2D semiconductor embedded resonant structures under coherent laser excitations.[5-8] Note that, the narrow linewidth here hints at the occurrence of a certain temporal coherence.[8] Furthermore, unlike the unpolarized resonant emission from MoS_2 flakes on microsphere,[38] the clear linear polarized behaviors have been observed in our case and in others' devices employing photonic crystal microcavities.[7, 34] Lastly, the cross-sectional intensity of resonant emission here has shown the Gaussian-beam profile, which is similar to the case from the microdisk cavity notch,[8] indicating the formation of spatial coherence.

Conclusions

In summary, we have demonstrated a white-light pumped resonant emission from a 2D semiconductor at room temperature, which is aiming at miniaturization of solar-pumped light sources for integrated photonics. Under the laser excitation, the narrow and polarized emission doublet has been found to form a Gaussian-like beam and propagates along the Z direction. With the white-light illumination, the narrow emitting component is attributed to resonant emission since it exhibits almost identical position, width, polarization, location, and spatial coherence with the ones obtained under the laser pumping. The extraordinary evolution of a spectral flipping signal to a single dip has been found in the response range of the designed fundamental mode, which directly reflects the competition of strongly correlated resonant absorption and emission. Our work represents an important step towards the realization of highly compact on-chip light sources or even solar lasers, which open new opportunities to develop solar or white-light powered photonic technologies.

Experimental Section

The microcavity device was fabricated by the combinational use of e-beam evaporation, micro-exfoliation, and dry transfer techniques. The 14.5 pairs of bottom-SiO_2/TiO_2 DBRs were firstly

deposited on a 300 nm-SiO_2/Si substrate *via* e-beam evaporation, which was followed by the preparation of a 1L-WS_2 embedded SiO_2 layer with a half-wavelength thickness. The deposition thicknesses of SiO_2 and TiO_2 in DBRs are 109 nm and 68 nm, respectively. The active medium of 1L-WS_2 was sandwiched with the upper and lower spacer layers of SiO_2 with the same thickness of ~100 nm. The capping section was made of 8.5 pairs of top-SiO_2/TiO_2 DBRs, being similar to the fabrication processes described somewhere else.[3]

PL measurements were carried out at room temperature with a confocal microscopic system (WITec, Alpha 300), in which the excitation laser of 488 nm was focused on the sample through a 50× objective lens (Nikon, NA = 0.55) with a spot size of 1.2 μm and the signals were collected with a grating of 600 grooves/mm. The X and Y directions in Fig. 1b are set to be parallel (0º) and perpendicular (90º) to the lower edge of the 1L-WS_2 flake, respectively. The solar light pumping was simulated by a white LED source and the Köhler illumination was used to realize the even white-light excitation in the sampling area. By appling an aperture in the optical path of incidence, the illumination area was limited in a spot diameter of ~85 μm. The normal reflection spectra were measured under the near-normal incidence by use of a 10× objective lens with NA=0.17. The confocal spectra and spatial mappings under white-light illumination were collected in the back-scattering configuration with the same 50× objective lens as the one used in the PL above. The excitation power density of the used white-light LED is ~ 0.09 W/cm^2, which is estimated by a thermal power meter. For spectral mappings in Figs 4c, 4e, 4f, and S8, the detection polarization configurations were set to along the X direction (0º) of the 1L-WS_2 flake and a scanning step size of 200 nm was employed. The PL line-scanning (in-plane) profiles (Figure S9 and 4d) crossing the flake center were performed under the unpolarized detection polarization and with a scanning step size of 300 nm. Angle-resolved reflection and PL measurements were performed by a customized microscopic system (Ideaoptic, ARM) together with a spectrograph (Andor, Kymera328i), in which a 100× objective lens (Olympus, NA=0.9) and an excitation laser of 532 nm were employed.

Supporting Information

Supporting Information is available from the Wiley Online Library or from the author.

Acknowledgements

Received: ((will be filled in by the editorial staff))

Revised: ((will be filled in by the editorial staff))

Published online: ((will be filled in by the editorial staff))

References

13

[1]   K. F. Mak, J. Shan, *Nat. Photonics* **2016**, 10, 216; G. Wang, A. Chernikov, M. M. Glazov, T. F. Heinz, X. Marie, T. Amand, B. Urbaszek, *Rev. Mod. Phys.* **2018**, 90, 021001.

[2]   S. F. Wu, S. Buckley, J. R. Schaibley, L. F. Feng, J. Q. Yan, D. G. Mandrus, F. Hatami, W. Yao, J. Vuckovic, A. Majumdar, X. D. Xu, *Nature* **2015**, 520, 69; Y. Z. Li, J. X. Zhang, D. D. Huang, H. Sun, F. Fan, J. B. Feng, Z. Wang, C. Z. Ning, *Nat. Nanotechnol.* **2017**, 12, 987; Y. Ye, Z. J. Wong, X. F. Lu, X. J. Ni, H. Y. Zhu, X. H. Chen, Y. Wang, X. Zhang, Nat Photonics 2015, 9, 733; O. Salehzadeh, M. Djavid, N. H. Tran, I. Shih, Z. Mi, *Nano Lett.* **2015**, 15, 5302.

[3]   J. Z. Shang, C. X. Cong, Z. L. Wang, N. Peimyoo, L. S. Wu, C. J. Zou, Y. Chen, X. Y. Chin, J. P. Wang, C. Soci, W. Huang, T. Yu, *Nat. Commun.* **2017**, 8, 543.

[4]   M. Koperski, K. Nogajewski, A. Arora, V. Cherkez, P. Mallet, J. Y. Veuillen, J. Marcus, P. Kossacki, M. Potemski, Nat Nanotechnol 2015, 10, 503; Y. M. He, G. Clark, J. R. Schaibley, Y. He, M. C. Chen, Y. J. Wei, X. Ding, Q. Zhang, W. Yao, X. D. Xu, C. Y. Lu, J. W. Pan, Nat Nanotechnol 2015, 10, 497; A. Srivastava, M. Sidler, A. V. Allain, D. S. Lembke, A. Kis, A. Imamoglu, *Nat. Nanotechnol.* **2015**, 10, 491.

[5]   C. Javerzac-Galy, A. Kumar, R. D. Schilling, N. Piro, S. Khorasani, M. Barbone, I. Goykhman, J. B. Khurgin, A. C. Ferrari, T. J. Kippenberg, *Nano Lett.* **2018**, 18, 3138.

[6]   R. Khelifa, P. Back, N. Flory, S. Nashashibi, K. Malchow, T. Taniguchi, K. Watanabe, A. Jain, L. Novotny, *Nano Lett.* **2020**, 20, 6155.

[7]   C. Husko, J. Kang, G. Moille, J. D. Wood, Z. Han, D. Gosztola, X. D. Ma, S. Combrie, A. De Rossi, M. C. Hersam, X. Checoury, J. R. Guest, *Nano Lett.* **2018**, 18, 6515.

[8]   J. C. Reed, A. Y. Zhu, H. Zhu, F. Yi, E. Cubukcu, *Nano Lett.* **2015**, 15, 1967.

[9]   C. Trovatello, A. Marini, X. Xu, C. Lee, F. Liu, N. Curreli, C. Manzoni, S. Dal Conte, K. Yao, A. Ciattoni, J. Hone, X. Zhu, P. J. Schuck, G. Cerullo, *Nat. Photonics* **2021**, 15, 6.

[10]   X. Lin, Y. Liu, K. Wang, X. Liu, Y. Yan, Y. J. Li, J. Yao, Y. S. Zhao, *Research* **2018**, 2018, 4164029; J. Zhang, W. Zhao, P. Yu, G. Yang, Z. Liu, *2D Mater.* **2020**, 7, 042002; J. Hernandez-Rueda, M. L. Noordam, I. Komen, L. Kuipers, *ACS Photonics* **2021**, 8, 550.

[11]   A. Goetzberger, J. Luther, G. Willeke, Sol Energ Mat Sol C 2002, 74, 1; M. A. Green, A. Ho-Baillie, H. J. Snaith, *Nat. Photonics* **2014**, 8, 506.

[12]   Z. J. Kiss, H. R. Lewis, R. C. Duncan, *Appl. Phys. Lett.* **1963**, 2, 93.

[13]   A. L. Golger, I. I. Klimovskiĭ, Soviet Journal of Quantum Electronics 1984, 14, 164.

[14]   R. Gorthala, M. Tidd, S. Lawless, *Sol. Energy* **2017**, 157, 629.

[15]   H. J. Han, S. B. Riffat, S. H. Lim, S. J. Oh, *Sol. Energy* **2013**, 94, 86.

[16]   S. Mehellou, D. W. Liang, J. Almeida, R. Bouadjemine, C. R. Vistas, E. Guillot, F. Rehouma, *Sol. Energy* **2017**, 155, 1059.

[17]   D. Lingfors, T. Volotinen, *Opt. Express* **2013**, 21, A642.

[18]   T. Masuda, M. Iyoda, Y. Yasumatsu, M. Endo, *Opt. Lett.* **2017**, 42, 3427.

[19]   G. Bjork, S. Machida, Y. Yamamoto, K. Igeta, *Phys. Rev. A* **1991**, 44, 669.

[20]   X. Liu, W. Bao, Q. Li, C. Ropp, Y. Wang, X. Zhang, *Phys. Rev. Lett.* **2017**, 119, 027403; Z. Sun, J. Gu, A. Ghazaryan, Z. Shotan, C. R. Considine, M. Dollar, B. Chakraborty, X. Liu, P. Ghaemi, S. Kéna-Cohen, V. M. Menon, *Nat. Photonics* **2017**, 11, 491.

[21]   A. Larsson, J. S. Gustavsson, in *VCSELs: Fundamentals, Technology and Applications of Vertical-Cavity Surface-Emitting Lasers*, (Ed: R. Michalzik), Springer Berlin Heidelberg, Berlin, Heidelberg **2013**, 119.

[22]   A. K. J. Vandoorn, M. P. Vanexter, J. P. Woerdman, *Electron Lett.* **1994**, 30, 1941.

[23]   K. D. Choquette, R. E. Leibenguth, *IEEE Photonic Tech. L.* **1994**, 6, 40.

[24]   M. Shimizu, F. Koyama, K. Iga, *Jpn. J. App. Phys.* **1988**, 27, 1774.

[25]   G. Khitrova, H. M. Gibbs, F. Jahnke, M. Kira, S. W. Koch, *Rev. Mod. Phys.* **1999**, 71, 1591.

[26]   H. Deng, H. Haug, Y. Yamamoto, *Rev. Mod. Phys.* **2010**, 82, 1489.

[27]   Y. Wang, X. Li, V. Nalla, H. Zeng, H. Sun, Advanced Functional Materials 2017, 27, 1605088; A. Haglund, J. S. Gustavsson, J. Vukusic, P. Modh, A. Larsson, *IEEE Photonic Tech. L.* **2004**, 16, 368.

[28]   C. Y. Huang, C. Zou, C. Y. Mao, K. L. Corp, Y. C. Yao, Y. J. Lee, C. W. Schlenker, A. K. Y. Jen, L. Y. Lin, *ACS Photonics* **2017**, 4, 2281.

[29]   S. A. Self, *Appl. Optics* **1983**, 22, 658.

[30]   I. D. W. Samuel, E. B. Namdas, G. A. Turnbull, *Nat. Photonics* **2009**, 3, 546.

[31]   S. E. Harris, Phys Rev Lett 1989, 62, 1033; A. Imamoğlu, S. E. Harris, *Opt. Lett.* **1989**, 14, 1344.

[32]   S. Bar-Ad, P. Kner, M. V. Marquezini, S. Mukamel, D. S. Chemla, *Phys. Rev. Lett.* **1997**, 78, 1363; M. Kroner, A. O. Govorov, S. Remi, B. Biedermann, S. Seidl, A. Badolato, P. M. Petroff, W. Zhang, R. Barbour, B. D. Gerardot, R. J. Warburton, K. Karrai, *Nature* **2008**, 451, 311.

[33]   C. Hsu, R. Frisenda, R. Schmidt, A. Arora, S. M. de Vasconcellos, R. Bratschitsch, H. S. J. van der Zant, A. Castellanos-Gomez, *Adv. Opt. Mater.* **2019**, 7, 1900239.

[34]   X. T. Gan, Y. D. Gao, K. F. Mak, X. W. Yao, R. J. Shiue, A. van der Zande, M. E. Trusheim, F. Hatami, T. F. Heinz, J. Hone, D. Englund, *Appl. Phys. Lett.* **2013**, 103, 181119 ; S. F. Wu, S. Buckley, A. M. Jones, J. S. Ross, N. J. Ghimire, J. Q. Yan, D. G. Mandrus, W. Yao, F. Hatami, J. Vuckovic, A. Majumdar, X. D. Xu, *2D Mater.* 2014, 1, 011001.

[35]   P. Rivera, T. K. Fryett, Y. Y. Chen, C. H. Liu, E. Ray, F. Hatami, J. Q. Yan, D. Mandrus, W. Yao, A. Majumdar, X. D. Xu, *2D Mater.* **2020**, 7, 015027.

[36]   S. Schwarz, S. Dufferwiel, P. M. Walker, F. Withers, A. A. P. Trichet, M. Sich, F. Li, E. A. Chekhovich, D. N. Borisenko, N. N. Kolesnikov, K. S. Novoselov, M. S. Skolnick, J. M. Smith, D. N. Krizhanovskii, A. I. Tartakovskii, *Nano Lett.* **2014**, 14, 7003.

[37]   J. C. Reed, S. C. Malek, F. Yi, C. H. Naylor, A. T. C. Johnson, E. Cubukcu, *Appl. Phys. Lett.* **2016**, 109, 193109.

[38]   Y. Mi, Z. P. Zhang, L. Y. Zhao, S. Zhang, J. Chen, Q. Q. Ji, J. P. Shi, X. B. Zhou, R. Wang, J. Shi, W. N. Du, Z. Y. Wu, X. H. Qiu, Q. Zhang, Y. F. Zhang, X. F. Liu, *Small* **2017**, 13, 1701694.

Table of contents

Bulk gain media, large-dimensional resonant cavities, and sizable focusing apparatuses seriously limit the application scope of solar-powered light sources. Particularly, the miniaturization of solar-driven photon emitters remains challenging. Here resonant emission from monolayer semiconductor has been demonstrated under the simulated solar illumination by a white-light emitting diode, which represents an exciting step toward on-chip solar-powered photonic circuits.
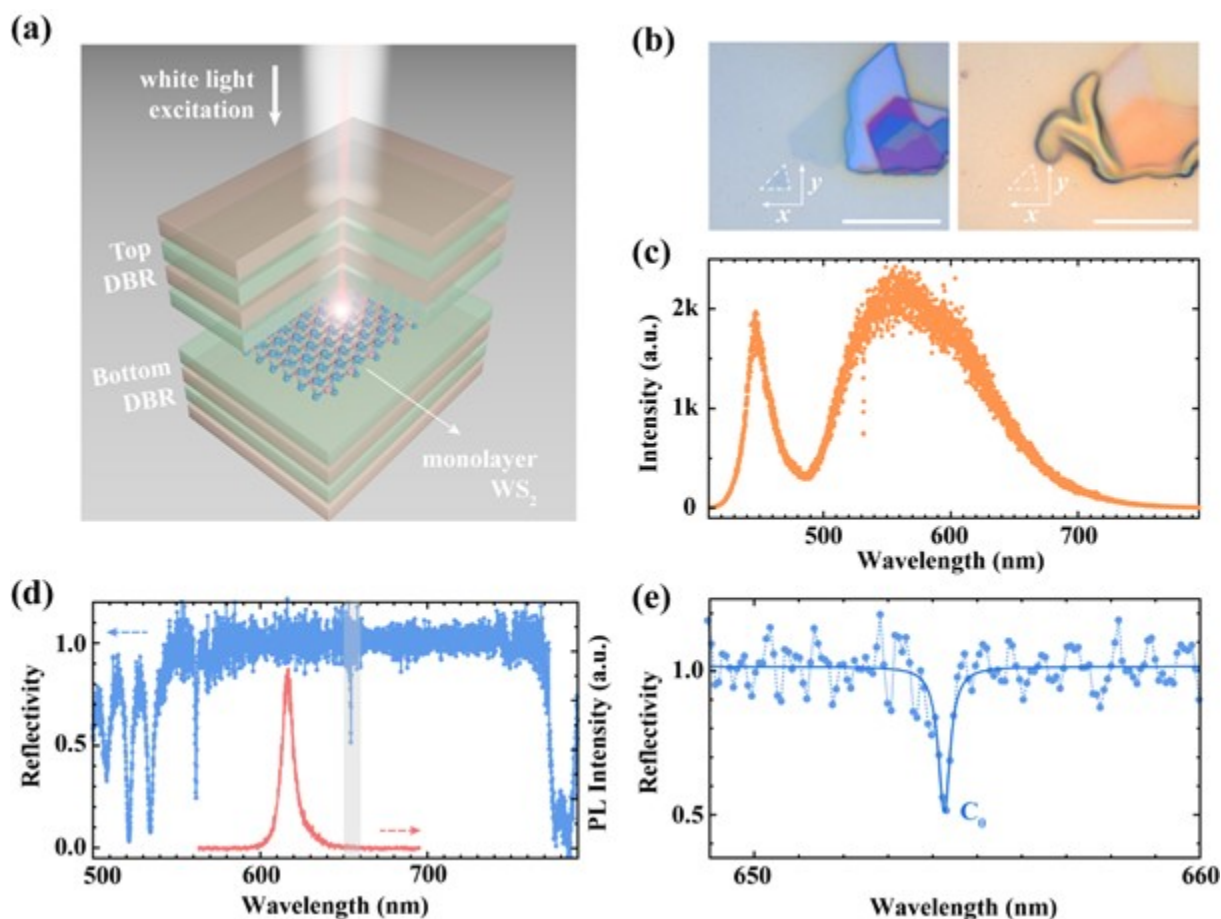
J. Shang, L. Wu, S. Feng, Y. Chen, H. Zhang, C. Cong*, W. Huang*, T. Yu*

Title: White-Light Driven Resonant Emission from a Monolayer Semiconductor

ToC figure
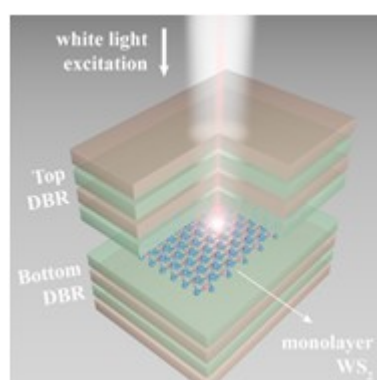
Figures and Captions

Fig. 1 Structure of a white-light driven resonant emitter, white-light source, and cavity mode. a, Schematic of a 2D semiconductor embedded resonant emitter, where 2DS, t-DBRs, and b-DBRs represent two-dimensional semiconductor, top and bottom distributed Bragg reflectors, respectively. **b**, Optical images of atomically thin WS_2 exfoliated on the bottom half cavity (left panel) and embedded in the full cavity (right panel), respectively, where $1L-WS_2$ region is indicated by the white dashed frame and scale bars represent 15μm. **c**, Illumination spectrum of the white-light source used to simulate solar light. **d**, Reflection spectrum (in blue) of the blank microcavity together with the PL

spectrum (the inset in red). **e**, Zoom-in normal reflection spectrum showing the cavity mode as well as single-Lorentzian fit curve (in blue).
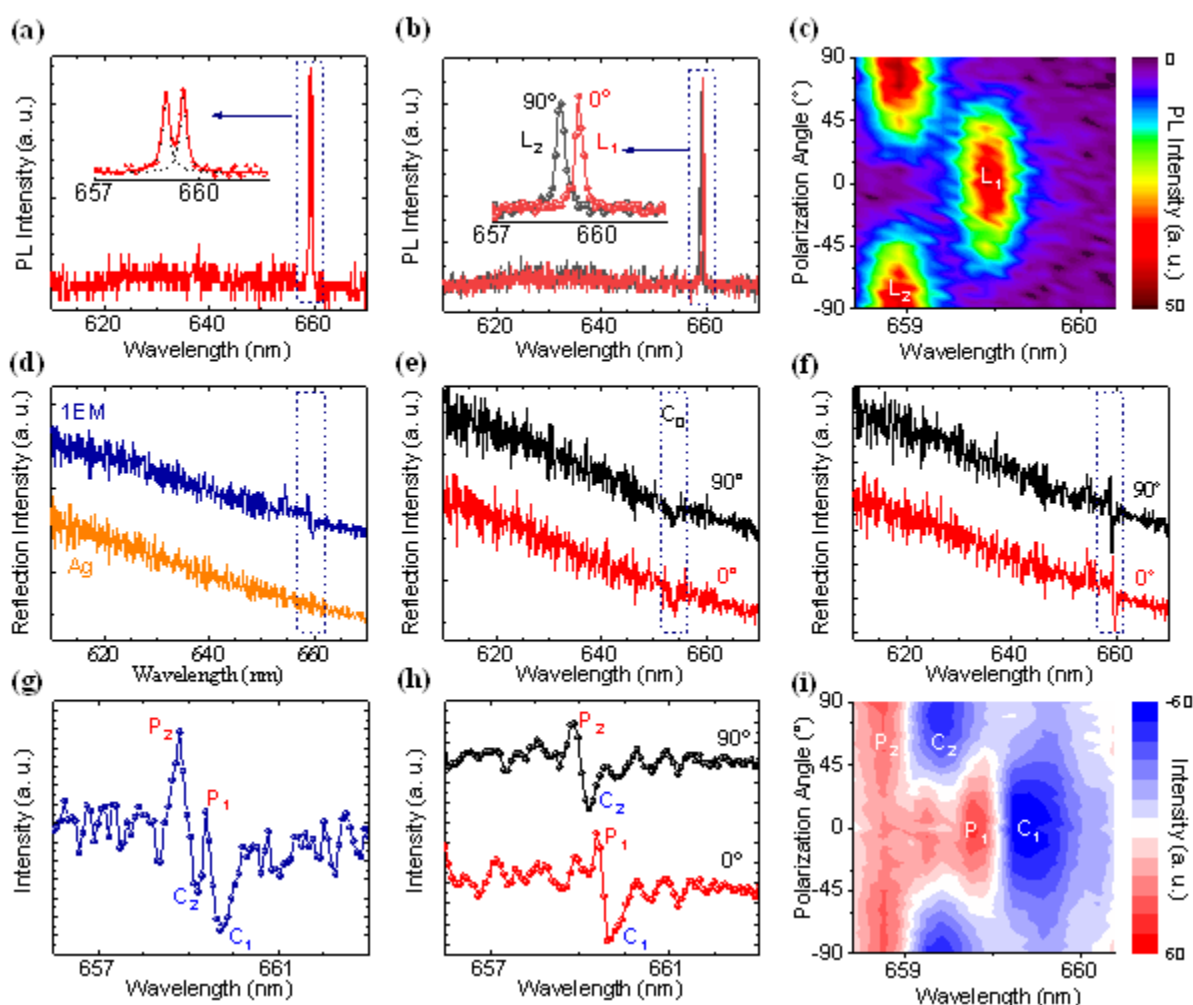

Fig. 2 Optical response under laser and white-light excitations. a, Unpolarized PL spectrum of 1L-WS$_2$ embedded microcavity taken under a 488 nm laser excitation with the enlarged doublet profile (the inset). **b**, Linearly polarized PL spectra taken at 0 and 90º, respectively. **c**, PL intensity *versus* polarization angle and wavelength. **d**, Unpolarized reflection signals of 1L-WS$_2$ embedded microcavity (denoted by 1EM) and the protected Ag mirror, respectively. **e**,**f**, Linearly polarized reflection signals of blank and 1L-WS$_2$ embedded microcavities, respectively. **g**, Zoom-in unpolarized

signals from (**d**). **h**, Zoom-in polarized signals after removing the backgrounds from (**f**). **i**, Reflected intensity *versus* polarization angle and wavelength.
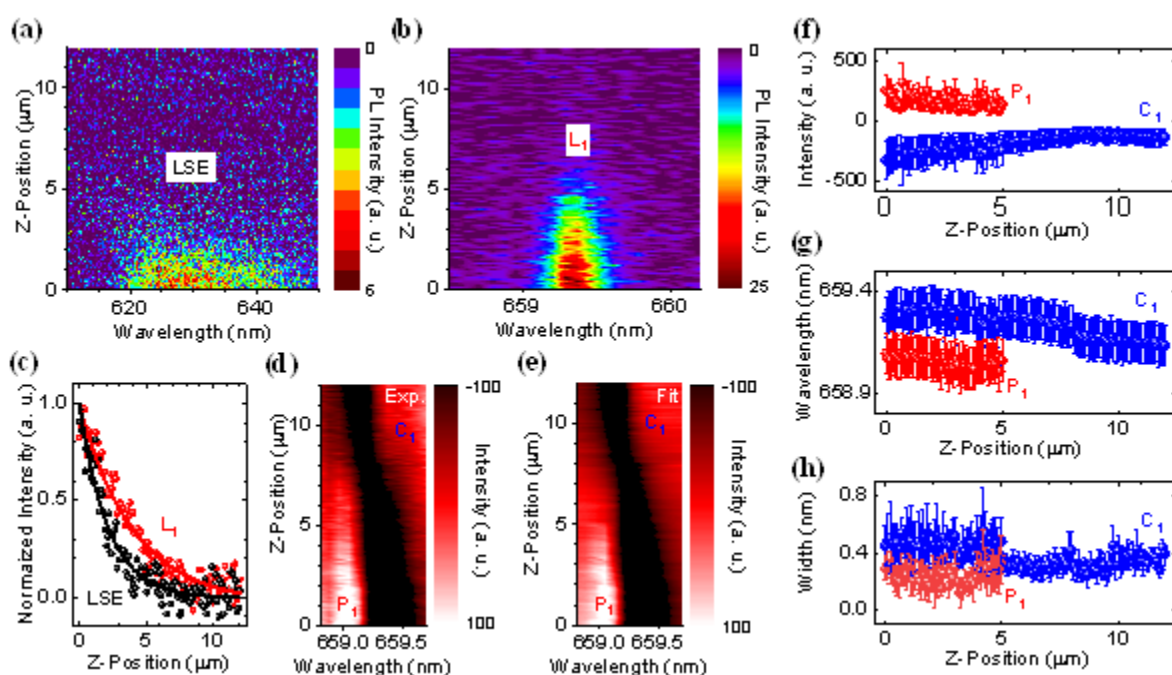
Fig. 3 Confocal optical response under laser and white-light excitations. a,**b**, Confocal LSE (**a**) and L_1 (**b**) maps taken along Z-direction from the device surface (*i.e.,* 0 μm) to the upward position of 12 μm. **c**, Normalized integrated intensities of LSE and L_1 along Z-direction. **d**,**e**, Experimental P_1-C_1 intensity (Exp.) after removal of the background and P_1-C_1 intensity reproduced by the combinational fitting (Fit) *versus* Z-position and wavelength, respectively. **f**,**g**,**h**, Integrated intensities, peak positions, and widths of C_1 and P_1 *versus* Z-position, respectively. Note that, (**a-c**) and (**d-h**) were obtained under laser and white-light excitations, respectively.
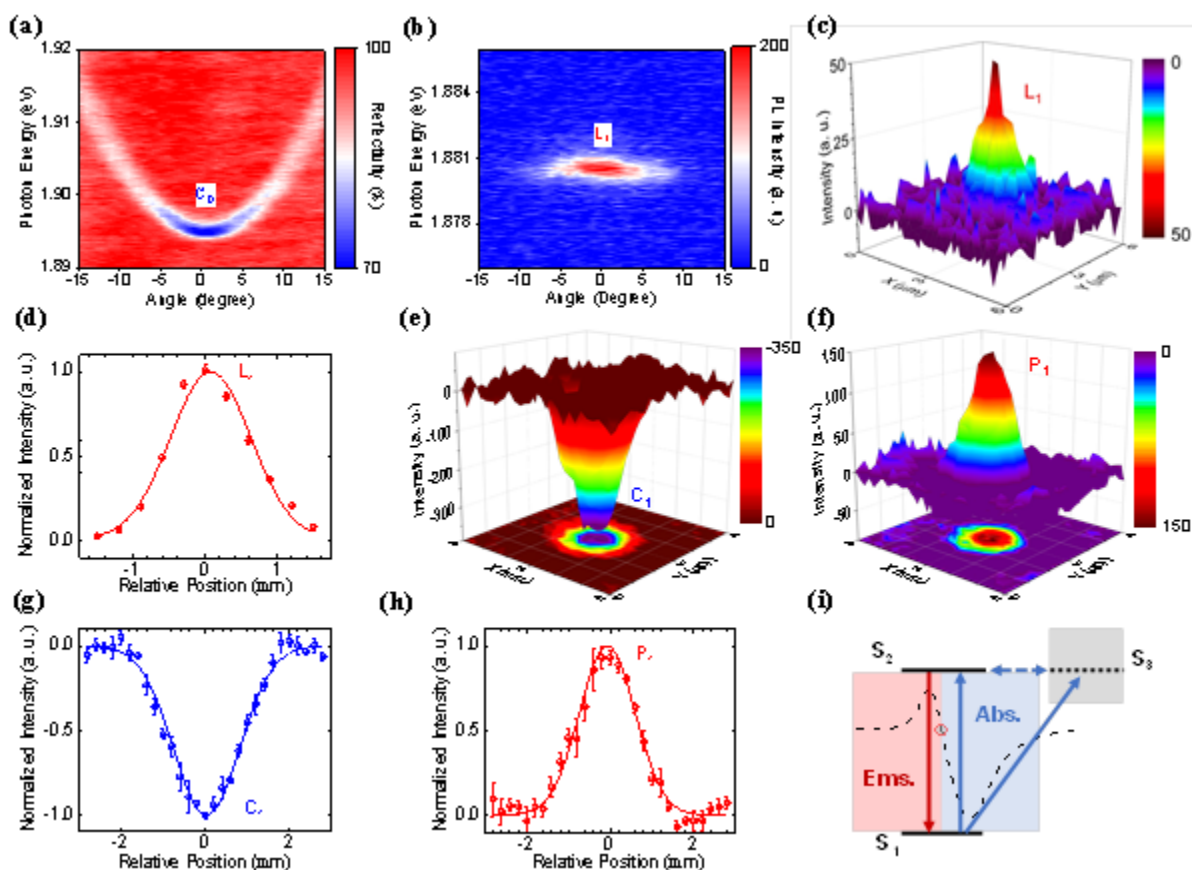
Fig. 4 Directionality and spatial coherence under laser and white-light excitations. a, Angle-resolved reflection map of a blank microcavity. **b**, Angle-resolved PL map of $1L\text{-}WS_2$ embedded microcavity. **c**, 3D plot of the integrated intensity of L_1. **d**, Analysis of the normalized intensity profile of L_1 across the center. **e,f**, 3D plots of integrated intensities of C_1 and P_1 under white-light illumination together with the corresponding 2D contour profiles, respectively. **g,h**, Analysis of the normalized intensity profile of C_1 and P_1 across the center, respectively. **i,** Schematic of the involved optical transitions of the flipping microscopic response under white-light illumination. The red circle indicates the crossing wavelength of a flipping signal.